World Scientific
www.worldscientific.com

THE UPPER BOUND PROPERTY FOR SOLID MECHANICS OF THE LINEARLY CONFORMING RADIAL POINT INTERPOLATION METHOD (LC-RPIM)

G. Y. ZHANG[*,†,‡], G. R. LIU[†,‡], T. T. NGUYEN[†] and C. X. SONG[†]

[†]*Centre for Advanced Computations in Engineering Science (ACES)*
Department of Mechanical Engineering, National University of Singapore
9 Engineering Drive 1, 117576, Singapore

[‡]*The Singapore — MIT Alliance (SMA), E4-04-10*
4 Engineering Drive 3, 117576, Singapore
[*]*smazg@nus.edu.sg*

X. HAN, Z. H. ZHONG and G. Y. LI

State Key Laboratory of Advanced Technology
for Vehicle Body Design & Manufacture
Hunan University, Changsha, 410082, P. R. China

It has been proven by the authors that both the upper and lower bounds in energy norm of the exact solution to elasticity problems can now be obtained by using the fully compatible finite element method (FEM) and linearly conforming point interpolation method (LC-PIM). This paper examines the upper bound property of the linearly conforming radial point interpolation method (LC-RPIM), where the Radial Basis Functions (RBFs) are used to construct shape functions and node-based smoothed strains are used to formulate the discrete system equations. It is found that the LC-RPIM also provides the upper bound of the exact solution in energy norm to elasticity problems, and it is much sharper than that of LC-PIM due to the decrease of stiffening effect. An effective procedure is also proposed to determine both upper and lower bounds for the exact solution without knowing it in advance: using the LC-RPIM to compute the upper bound, using the standard fully compatible FEM to compute the lower bound based on the same mesh for the problem domain. Numerical examples of 1D, 2D and 3D problems are presented to demonstrate these important properties of LC-RPIM.

Keywords: Meshfree methods; point interpolation method; radial basis functions; strain smoothing; error bound; elasticity.

1. Introduction

The finite element method (FEM) has been well developed and is now widely and routinely used to provide a numerical solution to engineering problems. However, to certify the solution or to provide an error bounds to the numerical solution of FEM

is far from routine. It is well known that the displacement-based fully compatible FEM model provides lower bound solution in energy norm to elasticity problems. It is, however, much more difficult to find an effective method to bound the exact solution from above for general problems in elasticity. Recently, the linearly conforming point interpolation method (LC-PIM) [Liu *et al.* (2005a)] has been developed using meshfree technique [Liu (2002)] combined with the FEM, and it has been found and proven that the LC-PIM can provide upper bound solution in energy norm for elasticity problems [Liu and Zhang (2007)]. In the LC-PIM, background cells of triangle elements are employed and simple linear interpolation is used to interpolate the displacement field, which is very similar but simpler than the practice in the FEM. Instead of using the compatible strain that is obtained from the strain–displacement relation, LC-PIM uses "smoothed" strain over smoothing cells of the nodes in the problem domain. The discretized system equations of LC-PIM are then constructed based on the "generalized" Galerkin weak form, which is derived from the Hellinger–Reissner's two-field variational principle. Solution of the LC-PIM model satisfies the equilibrium equations (free of body force) at any point in the entire problem domain, except on the interfaces of the smoothing cells. The displacement field in the LC-PIM is compatible in the global problem domain. However, the strains in the smoothing cells are not compatible in terms of satisfying the displacement–strain relations. Therefore, the LC-PIM is a "quasi"-equilibrium model that combines equilibrium model and compatible model [Liu and Zhang (2007)]. In a summary, the LC-PIM so constructed possesses some intrinsic properties (for problems with homogeneous essential boundary conditions):

- The LC-PIM is variationally consistent, and the generalized Galerkin weak form is a valid form for generating the discretized system equations.
- When the same mesh is used, the strain energy obtained from the LC-PIM solution is no-less than that from the FEM solution based on compatible displacement model.
- The LC-PIM solution (in energy norm) is no-less than that of exact solution except a few trivial cases.

Detailed proof on these important properties can be found in the recent paper by Liu and Zhang [2007].

The linearly conforming radial point interpolation method (LC-RPIM) was developed from the meshfree radial point interpolation method (RPIM) which was originally formulated based on the Galerkin weak form with shape functions constructed using radial point interpolation and a small set of nodes located in a local support domain [Wang and Liu (2000, 2002a)]. The unique feature of RPIM is that the shape functions possess the Delta function property, which allows straightforward imposition of point essential boundary conditions. Using the stabilized nodal integration scheme with strain smoothing operation proposed by Chen *et al.* [2001], Liu and his co-workers have developed the linearly conforming radial point

interpolation method (LC-RPIM) [Liu *et al.* (2006)]. In the LC-RPIM, radial basis functions (RBFs) augmented with linear polynomials are used to construct shape functions, which can ensure the reproduction of the linear field [Liu (2002); Liu and Gu (2005)]. The stabilized nodal integration scheme with strain smoothing is employed to perform the numerical integration. The LC-RPIM can guarantee linear exactness and monotonic convergence of the numerical solutions. Compared with the traditional RPIM using Gauss integration scheme, the LC-RPIM obtains higher convergence rate in terms of stress calculation.

A thorough theoretical study and intensive numerical investigation on the LC-PIM have found that smoothing operation in the process of the nodal integration scheme can provide sufficiently strong "softening" effects (compared to the stiffening effects introduced by the assumption of the displacement field) to the stiffness matrix of the discretized system equations. This finding reveals the fact that a numerical method with strain smoothing operation can provide upper bound solution in energy norm to elasticity problems [Liu and Zhang (2007)]. This finding has also naturally motivated us to further examine the solution bound property of the LC-RPIM, as the strain smoothing operation is also used in the LC-RPIM. This study has found and confirmed by a large number of examples the important fact that the LC-RPIM also possesses the upper bound property, and the bound is significantly sharper than that of LC-PIM. In this paper, we will first briefly introduce the formulae of the LC-RPIM, and then some important properties of the LC-RPIM are presented and examined. Finally, an intensive study using 1D, 2D and 3D examples will be conducted to demonstrate the properties of LC-RPIM.

2. Briefing on the Linearly Conforming Radial Point Interpolation Method (LC-RPIM)

The formulation in this paper will largely for 2D problems for the convenience and clarity of the presentation and without loss of generality. In our numerical study, however, examples of 1D, 2D and 3D will be presented. Details of the formulae for LC-RPIM can be found in the previous work [Liu *et al.* (2006)], and here we only give a briefing.

2.1. *Construction of RPIM shape functions*

To overcome the singularity problem of moment matrix which occurs in the polynomial point interpolation method formulae [Liu and Gu (1999, 2001)], radial basis functions were introduced and modified with real shape parameters to construct PIM shape functions [Wang and Liu (2000, 2002a)]. Using radial basis functions augmented with polynomials, a field variable function $u(\mathbf{x})$ can be approximated as follows:

$$u^h(\mathbf{x}) = \sum_{i=1}^{n} R_i(\mathbf{x})a_i + \sum_{j=1}^{m} P_j(\mathbf{x})b_j = \mathbf{R}^T(\mathbf{x})\mathbf{a} + \mathbf{P}^T(\mathbf{x})\mathbf{b}, \tag{1}$$

where $R_i(\mathbf{x})$ and $P_j(\mathbf{x})$ are radial basis functions and polynomial basis functions respectively, a_i and b_j are corresponding constants, n is the number of field nodes in the local support domain and m is the number of polynomial terms. When $m = 0$, pure RBFs are used. Otherwise, the RBF is augmented with m terms of polynomial basis functions. In the present work, the multi-quadrics RBF (MQ-RBF) [Hardy (1990)] is used.

$$R_i(\mathbf{x}) = (r_i^2 + (\alpha_c d_c)^2)^q, \tag{2}$$

where d_c is the average nodal spacing near the point of interest $\mathbf{x}$; α_c and q are two arbitrary real numbers of dimensionless parameters as suggested by Liu [2002], and r_i is the distance from the node (x_i, y_i) to the point of interest (x, y) which is defined as

$$r_i = \sqrt{(x - x_i)^2 + (y - y_i)^2}. \tag{3}$$

In Eq. (1), n nodes are used to construct the approximation, which are located in the local support domain of the point of interest. In the present work, a circular-shaped domain is used and the fields nodes locate inside will be chosen for the approximation. The dimension of the local support domain d_s, also the radius of the circular, is defined as

$$d_s = \alpha_s d_c, \tag{4}$$

where α_s is a positive real number of dimensionless size of the local support domain. In the present study, the following values of the parameters are used, i.e. $q = 1.03$, $\alpha_c = 4.0$ and $\alpha_s = 3.0$. These values have been found to perform well for most solid mechanics problems [Wang and Liu (2002b); Liu *et al.* (2005b)].

The constants in Eq. (1) can be determined by enforcing the field function to be satisfied at the n nodes within the local support domain of the point of interest $\mathbf{x}$. This leads to n linear equations, which can be expressed in the matrix form as

$$\mathbf{U}_s = \mathbf{R}_q \mathbf{a} + \mathbf{P}_m \mathbf{b}, \tag{5}$$

where $\mathbf{U}_s$ is the vector of function values,

$$\mathbf{U}_s = \{u_1 \quad u_2 \quad \cdots \quad u_n\}^T, \tag{6}$$

$\mathbf{R}_q$ is the moment matrix of RBFs,

$$\mathbf{R}_q = \begin{bmatrix} R_1(r_1) & R_2(r_1) & \cdots & R_n(r_1) \\ R_1(r_2) & R_2(r_2) & \cdots & R_n(r_2) \\ \cdots & \cdots & \cdots & \cdots \\ R_1(r_n) & R_2(r_n) & \cdots & R_n(r_n) \end{bmatrix}_{(n \times n)}, \tag{7}$$

$\mathbf{P}_m$ is the polynomial moment matrix,

$$
\mathbf{P}_m =
\begin{bmatrix}
1 & x_1 & y_1 & \cdots & p_m(\mathbf{x}_1) \\
1 & x_2 & y_2 & \cdots & p_m(\mathbf{x}_2) \\
\cdots & \cdots & \cdots & \cdots & \cdots \\
1 & x_n & y_n & \cdots & p_m(\mathbf{x}_n)
\end{bmatrix}_{(n \times m)},
\tag{8}
$$

$\mathbf{a}$ and $\mathbf{b}$ are vectors of coefficients for RBFs and polynomial basis functions respectively.

$$
\begin{aligned}
\mathbf{a}^T &= \{a_1 \quad a_2 \quad \cdots \quad a_n\}, \\
\mathbf{b}^T &= \{b_1 \quad b_2 \quad \cdots \quad b_n\}.
\end{aligned}
\tag{9}
$$

As there are $n + m$ variables in Eq. (5), the additional m equations should be added by using the following constraint conditions [Golberg *et al.* (1999)].

$$
\sum_{i=1}^{n} p_j(\mathbf{x}_i)a_i = \mathbf{P}_m^T \mathbf{a} = 0, \quad j = 1, 2, \ldots, m.
\tag{10}
$$

Combining Eqs. (5) and (10) yields the following set of equations in the matrix form

$$
\tilde{\mathbf{U}}_s =
\begin{bmatrix}
\mathbf{U}_s \\
\mathbf{0}
\end{bmatrix}
=
\begin{bmatrix}
\mathbf{R}_q & \mathbf{P}_m \\
\mathbf{P}_m^T & \mathbf{0}
\end{bmatrix}
\begin{Bmatrix}
\mathbf{a} \\
\mathbf{b}
\end{Bmatrix}
= \mathbf{G}\mathbf{a}_0.
\tag{11}
$$

Solving Eq. (11), we have

$$
\begin{Bmatrix}
\mathbf{a} \\
\mathbf{b}
\end{Bmatrix}
= \mathbf{G}^{-1}\tilde{\mathbf{U}}_s.
\tag{12}
$$

Equation (1) can be rewritten as

$$
u^h(\mathbf{x}) = \mathbf{R}^T(\mathbf{x})\mathbf{a} + \mathbf{P}^T(\mathbf{x})\mathbf{b} = \{\mathbf{R}^T(\mathbf{x}) \quad \mathbf{P}^T(\mathbf{x})\}
\begin{Bmatrix}
\mathbf{a} \\
\mathbf{b}
\end{Bmatrix}.
\tag{13}
$$

Substituting Eq. (12) into Eq. (13) yields

$$
u^h(\mathbf{x}) = \{\mathbf{R}^T(\mathbf{x}) \quad \mathbf{P}^T(\mathbf{x})\}\mathbf{G}^{-1}\tilde{\mathbf{U}}_s = \tilde{\boldsymbol{\Phi}}^T(\mathbf{x})\tilde{\mathbf{U}}_s,
\tag{14}
$$

where the RPIM shape functions can be expressed as

$$
\begin{aligned}
\tilde{\boldsymbol{\Phi}}^T(\mathbf{x}) &= \{\mathbf{R}^T(\mathbf{x}) \quad \mathbf{P}^T(\mathbf{x})\}\mathbf{G}^{-1} \\
&= \{\varphi_1(x) \quad \varphi_2(x) \quad \cdots \quad \varphi_n(x) \quad \varphi_{n+1}(x) \quad \cdots \quad \varphi_{n+m}(x)\}.
\end{aligned}
\tag{15}
$$

Finally, the RPIM shape functions corresponding to the nodal values are obtained as

$$
\boldsymbol{\Phi}^T(\mathbf{x}) = \{\varphi_1(\mathbf{x}) \quad \varphi_2(\mathbf{x}) \quad \cdots \quad \varphi_n(\mathbf{x})\}.
\tag{16}
$$

Then Eq. (14) can be rewritten as

$$u^h(\mathbf{x}) = \mathbf{\Phi}^T(\mathbf{x})\mathbf{U}_s. \tag{17}$$

The derivatives of $u(\mathbf{x})$ are easily obtained as

$$u_l^h(\mathbf{x}) = \mathbf{\Phi}_l^T(\mathbf{x})\mathbf{U}_s, \tag{18}$$

where l denotes the coordinate x or y, and the comma denotes a partial differentiation with respect to the indicated spatial coordinate that follows.

2.2. *Discretized system equations*

It has been proved that the generalized Galerkin weak form, which is derived from the Hellinger–Reissner's two-field variational principle, is a valid weak form for LC-PIM [Liu and Zhang (2007)]. In the LC-RPIM, we first assume that the displacement is approximated using Eq. (17), and then assume the strain using the assumed displacement field as $\widehat{\varepsilon}(\mathbf{u})$. In the same way, any assumed displacement $\mathbf{u}$ and the corresponding assumed strain $\widehat{\varepsilon}(\mathbf{u})$ satisfies the generalized Galerkin weak form as follows:

$$\int_\Omega \delta(\widehat{\varepsilon}(\mathbf{u}))^T \mathbf{D}(\widehat{\varepsilon}(\mathbf{u}))d\Omega - \int_\Omega \delta\mathbf{u}^T\mathbf{b}d\Omega - \int_{\Gamma_t} \delta\mathbf{u}^T\hat{\mathbf{t}}d\Gamma = 0 \tag{19}$$

Substituting Eq. (17) into Eq. (19), a set of discretized system equations can be obtained in the following matrix form:

$$\widehat{\mathbf{K}}\widehat{\mathbf{d}} = \widehat{\mathbf{f}}. \tag{20}$$

In the process of obtaining Eq. (20), the nodal integration scheme with strain smoothing operation is used to perform the numerical integration over the problem domain Ω.

2.3. *Nodal integration with strain smoothing*

A node-based integration is used in the present method and the problem domain Ω is divided into smoothing domains $\Omega = \Omega_1 \cup \Omega_2 \cup \cdots \cup \Omega_N$ and $\Omega_i \cap \Omega_j = \varnothing$, $i \neq j$, in which N is the number of total field nodes. Background cells of triangles are used and the smoothing domain Ω_k for node k is formed by connecting sequentially the mid-edge-point to the centroids of the surrounding triangles of the node (shown in Fig. 1).

Introducing the nodal integration scheme, the entries of the stiffness matrix $\widehat{\mathbf{K}}$ can be represented as

$$\widehat{\mathbf{K}}_{ij} = \sum_{k=1}^N \widehat{\mathbf{K}}_{ij(k)}, \tag{21}$$
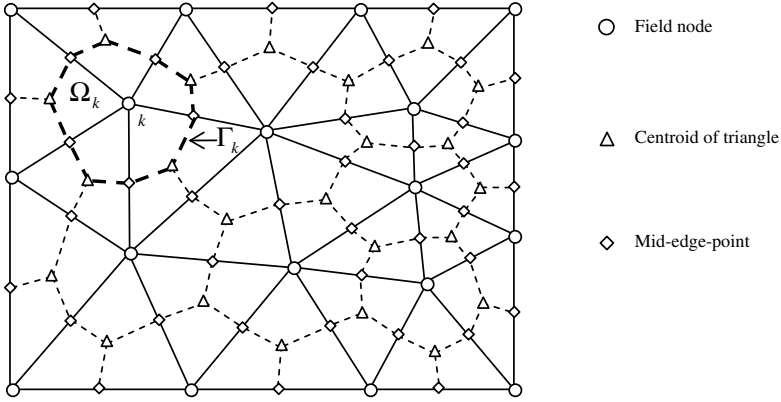
Fig. 1. Illustration of background triangular cells and the smoothing domain for each node (The smoothing domain is created by sequentially connecting the controids with the mid-edge-points of the surrounding triangles of this node).

where $\widehat{\mathbf{K}}_{ij(k)}$ is the stiffness matrix of node k which is calculated as

$$\widehat{\mathbf{K}}_{ij(k)} = \int_{\Omega_k} \widehat{\mathbf{B}}_i^{\mathrm{T}} \mathbf{D} \widehat{\mathbf{B}}_j d\Omega = \widehat{\mathbf{B}}_i^{\mathrm{T}} \mathbf{D} \widehat{\mathbf{B}}_j A_k, \qquad (22)$$

where $\widehat{\mathbf{B}}$ is the smoothed strain matrix, $\mathbf{D}$ is the matrix of material constants and A_k is the area of the smoothing domain of node k.

The entries of the force vector $\widehat{\mathbf{f}}$ in Eq. (20) can be expressed as

$$\widehat{\mathbf{f}}_i = \sum_{k \in N_{\mathrm{infl}}} \widehat{\mathbf{f}}_{i(k)}, \qquad (23)$$

where N_{infl} is the number of nodes in the influence domain of node k (including node k) or those nodes whose shape function support cover node k, $\widehat{\mathbf{f}}_{i(k)}$ can be further expressed as

$$\widehat{\mathbf{f}}_{i(k)} = \int_{\Gamma_{t(k)}} \mathbf{\Phi}_i \hat{\mathbf{t}} d\Gamma + \int_{\Omega_{(k)}} \mathbf{\Phi}_i \mathbf{b} d\Omega. \qquad (24)$$

A node-based strain smoothing operation is now applied at each node to obtain

$$\widehat{\boldsymbol{\varepsilon}}_k \equiv \widehat{\boldsymbol{\varepsilon}}(\mathbf{x}_k) = \int_{\Omega_k} \boldsymbol{\varepsilon}(\mathbf{x}) \widehat{\mathbf{W}}(\mathbf{x} - \mathbf{x}_k) d\Omega, \qquad (25)$$

where $\widehat{\boldsymbol{\varepsilon}}_k$ is the smoothed strain for node k, $\widehat{\mathbf{W}} = \lfloor \widehat{W} \quad \widehat{W} \quad \widehat{W} \rfloor$ is a diagonal matrix of smoothing function $\widehat{W}$. For simplicity, the smoothing function is taken as

$$\widehat{W}(\mathbf{x} - \mathbf{x}_k) = \begin{cases} 1/A_k, & \mathbf{x} \in \Omega_k \\ 0, & \mathbf{x} \notin \Omega_k, \end{cases} \qquad (26)$$

where A_k is the area of smoothing domain for node k.

Substituting Eq. (26) into Eq. (25) and integrating by parts, we arrive at

$$\widehat{\varepsilon}_k = \frac{1}{A_k} \int_{\Omega_k} \varepsilon(\mathbf{x}) d\Omega = \frac{1}{A_k} \int_{\Gamma_k} \mathbf{L}_n \mathbf{u}(\mathbf{x}) d\Gamma = \widehat{\varepsilon}_k(\mathbf{u}), \tag{27}$$

where Γ_k is the boundary of the smoothing domain for node k, $\mathbf{L}_n$ is the matrix of the outward normal vector on Γ_k, expressed as follows:

$$\mathbf{L}_n = \begin{bmatrix} n_x & 0 \\ 0 & n_y \\ n_y & n_x \end{bmatrix}. \tag{28}$$

Substituting Eq. (17) into Eq. (27), the smoothed strain can be expressed in the matrix form as follows:

$$\widehat{\varepsilon}_k = \sum_{i \in N_{\text{infl}}} \widehat{\mathbf{B}}_i(\mathbf{x}_k) \mathbf{U}_i, \tag{29}$$

where $\widehat{\mathbf{B}}_i(\mathbf{x}_k)$ is the smoothed strain matrix which is expressed as

$$\widehat{\mathbf{B}}_i(\mathbf{x}_k) = \begin{bmatrix} \widehat{b}_{ix}(\mathbf{x}_k) & 0 \\ 0 & \widehat{b}_{iy}(\mathbf{x}_k) \\ \widehat{b}_{iy}(\mathbf{x}_k) & \widehat{b}_{ix}(\mathbf{x}_k) \end{bmatrix}, \tag{30}$$

where the elements of the smoothed strain matrix are calculated by using Gauss integration along each segment of boundary Γ_k.

$$\widehat{b}_{il} = \frac{1}{A_k} \sum_{m=1}^{N_s} \left[\sum_{n=1}^{N_g} w_n \varphi_i(\mathbf{x}_{mn}) n_l(\mathbf{x}_m) \right] \quad (l = x, y), \tag{31}$$

where N_s is the number of segments of the boundary Γ_k, N_g is the number of Gauss points used in each segment, w_n is the corresponding weight number of Gauss integration scheme, and n_l is the unit outward normal corresponding to each segment on the smoothing domain boundary.

3. Properties of LC-RPIM

Some important properties of LC-RPIM have been found and proved in the present work.

Property 1: *Variationally consistent*

Proof. The LC-RPIM is variationally consistent, in which the smoothed strain is used instead of the compatible strain. To examine the variational consistency, we start with the Hellinger–Reissner's two-field variational principle [Wu (1982)]:

$$J(\mathbf{u}, \varepsilon) = -\int_{\Omega} \frac{1}{2} \varepsilon^T \mathbf{D} \varepsilon d\Omega - \int_{\Omega} (\mathbf{L}_d^T \boldsymbol{\sigma} + \mathbf{b})^T \mathbf{u} d\Omega + \int_{\Gamma_u} \mathbf{t}^T \widehat{\mathbf{u}} d\Gamma - \int_{\Gamma_t} (\widehat{\mathbf{t}} - \mathbf{t})^T \mathbf{u} d\Gamma, \tag{32}$$

where ε is the assumed strain vector that is independent of $\mathbf{u}$, the stresses $\boldsymbol{\sigma}$ is dependent on the strains through the stress-strain relation $\boldsymbol{\sigma} = \boldsymbol{D}\varepsilon$, $\mathbf{t}$ is the traction on the boundary that is depending on the stresses $\boldsymbol{\sigma}$ in the form of $\mathbf{L}_n^T \boldsymbol{\sigma} = \mathbf{t}$, $\hat{\mathbf{u}}$ and $\hat{\mathbf{t}}$ are prescribed displacement and traction along the boundaries and $\mathbf{L}_d$ is a matrix of differential operator defined as

$$\mathbf{L}_d = \begin{bmatrix} \dfrac{\partial}{\partial x} & 0 \\[2mm] 0 & \dfrac{\partial}{\partial y} \\[2mm] \dfrac{\partial}{\partial y} & \dfrac{\partial}{\partial x} \end{bmatrix}. \tag{33}$$

Using the Green's divergence theorem and invoking Eq. (27), we have the following function of single displacement variable in the form of

$$J(\mathbf{u}) = -\int_\Omega \frac{1}{2}(\widehat{\boldsymbol{\varepsilon}}(\mathbf{u}))^T \mathbf{D}(\widehat{\boldsymbol{\varepsilon}}(\mathbf{u}))d\Omega - \int_\Omega \mathbf{b}^T \mathbf{u}d\Omega$$

$$- \int_{\Gamma_t} \hat{\mathbf{t}}^T \mathbf{u}d\Gamma + \int_\Omega \widehat{\boldsymbol{\varepsilon}}(\mathbf{u})^T \mathbf{D}\varepsilon(\mathbf{u})d\Omega. \tag{34}$$

Now we examine the last term in the above equation.

$$\int_\Omega \widehat{\boldsymbol{\varepsilon}}^T \mathbf{D}\varepsilon d\Omega = \int_\Omega \widehat{\boldsymbol{\varepsilon}}^T \mathbf{D}(\mathbf{L}_d\mathbf{u})d\Omega = \sum_{k=1}^N \int_{\Omega_k} \widehat{\boldsymbol{\varepsilon}}_k^T \mathbf{D}(\mathbf{L}_d\mathbf{u})d\Omega \tag{35}$$

Note that due to the smoothing operation, the assumed strains $\widehat{\boldsymbol{\varepsilon}}_k$ are constants in Ω_k. Using Green's divergence theorem for each smoothing domain Ω_k, we obtain

$$\int_\Omega \widehat{\boldsymbol{\varepsilon}}^T \mathbf{D}\varepsilon d\Omega = \sum_{k=1}^N \left[\int_{\Gamma_k} (\widehat{\boldsymbol{\varepsilon}}_k^T \mathbf{D})(\mathbf{L}_n\mathbf{u})d\Gamma - \int_{\Omega_k} \underbrace{(\mathbf{L}_d^T(\widehat{\boldsymbol{\varepsilon}}_k^T \mathbf{D}))^T}_{=0,\,\text{in }\Omega_k} \mathbf{u}d\Omega \right]$$

$$= \sum_{k=1}^N \int_{\Gamma_k} \widehat{\boldsymbol{\varepsilon}}_k^T \mathbf{D}(\mathbf{L}_n\mathbf{u})d\Gamma. \tag{36}$$

Again since $\widehat{\boldsymbol{\varepsilon}}_k$ is constant in Ω_k and invoking Eq. (27), we arrive at

$$\int_\Omega \widehat{\boldsymbol{\varepsilon}}^T \mathbf{D}\varepsilon d\Omega = \sum_{k=1}^N (\widehat{\boldsymbol{\varepsilon}}_k^T \mathbf{D}) \int_{\Gamma_k} (\mathbf{L}_n\mathbf{u})d\Gamma = \sum_{k=1}^N \widehat{\boldsymbol{\varepsilon}}_k^T \mathbf{D}\widehat{\boldsymbol{\varepsilon}}_k A_k = \int_\Omega \widehat{\boldsymbol{\varepsilon}}^T \mathbf{D}\widehat{\boldsymbol{\varepsilon}} d\Omega. \tag{37}$$

Equation (37) means that LC-RPIM satisfies the orthogonal condition:

$$\int_\Omega \widehat{\boldsymbol{\varepsilon}}^T \mathbf{D}\varepsilon d\Omega = \int_\Omega \widehat{\boldsymbol{\varepsilon}}^T \mathbf{D}\widehat{\boldsymbol{\varepsilon}} d\Omega, \tag{38}$$

which implies that LC-RPIM is variationally consistent. $\qquad\square$

Substituting the above equation into Eq. (34), then the generalized Galerkin weak form can be obtained as expressed in Eq. (19).

Property 2: *Upper bound property*

We now state that the LC-RPIM solution (in energy norm) is always no-less than that of displacement-based fully compatible finite element method (FEM), and is no-less than that of exact solution for problems with homogeneous essential boundary conditions except the following trivial cases where there is no sufficient smoothing operations.

One of such a trivial case is that when only one element is used. In this case, only one element participates in smoothing, which does not have any smoothing effects, and hence the LC-RPIM obtains same solution as the FEM.

The proof and detailed examination of above statement can be very similar to that for the LC-PIM. We, therefore, omit it here and refer the reader to the recent paper by Liu and Zhang [2007].

Property 3: *Tightness of the bound*

The upper bound provided by the LC-RPIM solution is much tighter than that of the LC-PIM using linear shape functions.

This property can be understood intuitively by the following arguments: the smoothing operation provides a "softening" effect to the solids or structures and the use of any compatible shape functions provide a "stiffening" effect to the model. Compared with the linear shape functions used in the LC-PIM, the RPIM shape functions used in the LC-RPIM are of higher order which reduces the "stiffening" effects to the model. Therefore, the upper bound provided by the LC-RPIM model is tighter than that of the LC-PIM using linear shape functions. Detailed discussion on the softening and stiffening effects to a numerical model using strain smoothing operation can be found in the previous work [Liu and Zhang (2007)].

4. Numerical Examples

A number of 1D, 2D and 3D numerical examples are studied in this section. Materials of the problems are linear elastic and units used are based on international standard unit system unless specially mentioned.

4.1. *1D bar problem*

A 1D bar problem with length L and uniform cross-sectional area A is considered. As shown in Fig. 2, the bar is fixed at the left end and subjected to a uniform body
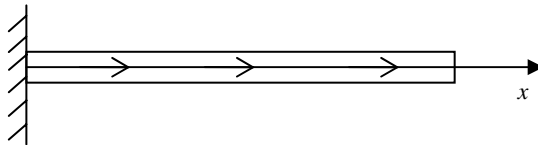

Fig. 2. One-dimensional bar subjected to a uniformly distributed body force.

force b. Values of the parameters as taken as $L = 1$, $A = 1$, $b = 1$ and $E = 1$. Governing equation and boundary conditions are expressed as

$$E\frac{d^2u}{dx^2} + 1 = 0,$$

$$u(x = 0) = 0, \tag{39}$$

$$\sigma(x = 1) = 0.$$

The exact solution can be calculated as follows

$$u_0(x) = -\frac{1}{2E}x^2 + \frac{1}{E}x. \tag{40}$$

We study this problem using FEM, LC-PIM and present LC-RPIM with 10 models of uniformly distributed nodes. The computed values of strain energy are plotted in Fig. 3 against the increase of degree of freedoms, together with the reference solution of strain energy which is calculated using the exact solution in Eq. (40). The figure shows that LC-PIM provides an upper bound solution on strain energy when the number of nodes is bigger than 2, while the FEM gives a lower bound. This result is consistent with previous work [Liu and Zhang (2007)]. Furthermore, the LC-RPIM is found to possess an upper bound property similar as LC-PIM, i.e. the strain energy of LC-RPIM solution is always bigger than the exact one and approaches to it from above monotonically. Compared with the LC-PIM, it has also been found that the present LC-RPIM is much tighter than the LC-PIM for the same problem by using same nodes distributions. This simple 1D problem has confirmed the properties of the LC-RPIM.
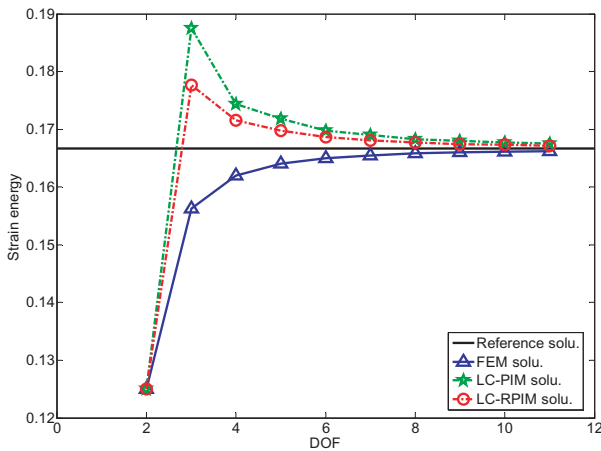

Fig. 3. Upper bound solution obtained using the LC-RPIM and LC-PIM for the 1D bar problem. The lower bound solution is obtained using the FEM with linear elements.

4.2. *2D cantilever beam*

A two-dimensional problem of a cantilever beam is now studied, which is of length L, height D and unit thickness. The beam is fixed at the left end and subjected to a parabolic traction at the right end as shown in Fig. 4. The analytical solution based on the plane stress theory is available as follows [Timoshenko and Goodier (1970)].

$$u_x = -\frac{py}{6EI}\left[(6L - 3x)x + (2 + \nu)\left(y^2 - \frac{D^2}{4}\right)\right], \tag{41}$$

$$u_y = \frac{p}{6EI}\left[3\nu y^2(L - x) + (4 + 5\nu)\frac{D^2 x}{4} + (3L - x)x^2\right], \tag{42}$$

$$\sigma_{xx} = -\frac{p(L - x)y}{I}, \tag{43}$$

$$\sigma_{yy} = 0, \tag{44}$$

$$\sigma_{xy} = \frac{p}{2I}\left[\frac{D^2}{4} - y^2\right], \tag{45}$$

where I is the moment of the inertia given as $I = D^3/12$. The parameters used in this problem are taken as $E = 3.0 \times 10^7$, $v = 0.3$, $L = 50$, $D = 10$ and $P = -1000$.

First we study the convergence property of the LC-RPIM and compared with the FEM and LC-PIM. Four models with regularly distributed nodes (105, 369, 793 and 1377 nodes) are used for all these methods. Errors in displacement and energy norms are calculated according to the following equations.

$$e_d = \sqrt{\frac{\sum\limits_{i=1}^{n}(u_i^{\text{exact}} - u_i^{\text{numerical}})^2}{\sum\limits_{i=1}^{n}(u_i^{\text{exact}})^2}} \tag{46}$$

$$e_e = \frac{1}{A}\sqrt{\frac{1}{2}\int_\Omega (\varepsilon^{\text{exact}} - \varepsilon^{\text{numerical}})^T \mathbf{D}(\varepsilon^{\text{exact}} - \varepsilon^{\text{numerical}})\, d\Omega} \tag{47}$$
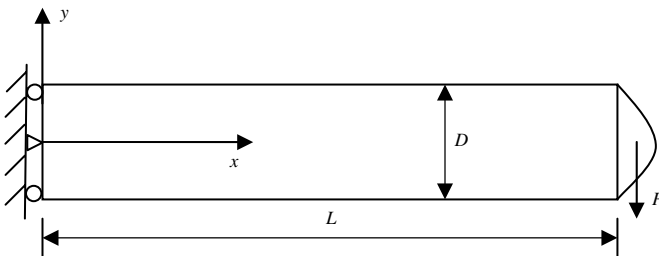

Fig. 4. A two-dimensional cantilever solid subjected to a parabolic traction on the right edge.

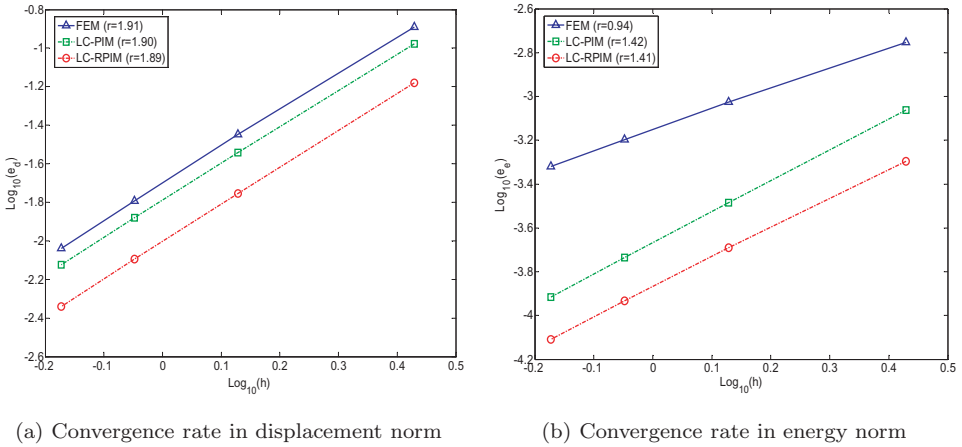(a) Convergence rate in displacement norm   (b) Convergence rate in energy norm

Fig. 5. Comparison of convergence rate between the linear FEM, the LC-PIM and the LC-RPIM via the 2D cantilever beam.

Figure 5 shows the convergence situation in terms of displacement error and energy error. It can be observed that the LC-RPIM and LC-PIM obtain similar convergence rate and accuracy in displacement compared with the linear FEM. For the results in energy norm, similar as LC-PIM, LC-RPIM is more accurate and achieves much higher convergence rate than the linear FEM.

Based on the discussion in the previous work [Liu and Zhang (2007)], the LC-RPIM behaves as a combination of equilibrium model and compatible model. The displacement fields in the LC-RPIM are compatible in the global problem domain, but the strains in the smoothing domains are obtained using Eq. (29) and hence will not be compatible in terms of satisfying the displacement-strain relations. On the other hand, the LC-RPIM satisfies the equilibrium equations (free of body force) at any point within the smoothing domain but only the displacement compatibility is ensured on the interfaces of the smoothing domains. It is known that the convergence rate in energy norm of a fully compatible model for linear field assumed is, in theory, 1.0; and for a fully equilibrium model, the convergence rate in energy norm should be, in theory, 2.0. Therefore, the convergence rate in energy norm for the present LC-RPIM should be, in theory, between 1.0 and 2.0, which is similar as the performance of LC-PIM. Figure 5 shows that the convergence rates in energy norm for the LC-PIM and LC-RPIM are 1.42 and 1.41 respectively, which has confirmed the theory.

Figure 6 shows the convergence status of the strain energies against the increase of Degree of Freedom (DOF) for all the three methods used in this problem, i.e. FEM, LC-PIM and LC-RPIM. The reference value of strain energy is calculated using the analytical solutions of stress components. It can be observed again that both the LC-RPIM and LC-PIM provide upper bound solutions in energy norm while the FEM gives a lower bound solution. Compared with the LC-PIM,
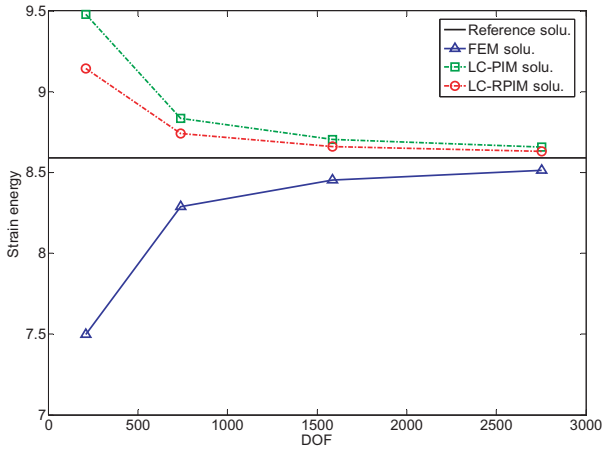
Fig. 6. Upper bound solution obtained using the LC-RPIM and LC-PIM for the 2D cantilever beam. The lower bound solution is obtained using the FEM with linear elements.

the LC-RPIM is tighter to the reference solution. This benchmark 2D problem has again confirmed the properties of the LC-RPIM which have been discussed in the previous section.

4.3. 2D infinite plate with a circular hole

An infinite two-dimensional plate with a central circular hole and subjected to a unidirectional tensile is studied. Due to the two-fold symmetry, one quarter of the plate is modeled with the dimensions of b in both x- and y-directions (as shown in Fig. 7). Symmetry conditions are imposed on the left and the bottom edges. The analytical solution of stress components is available as follows [Timoshenko and
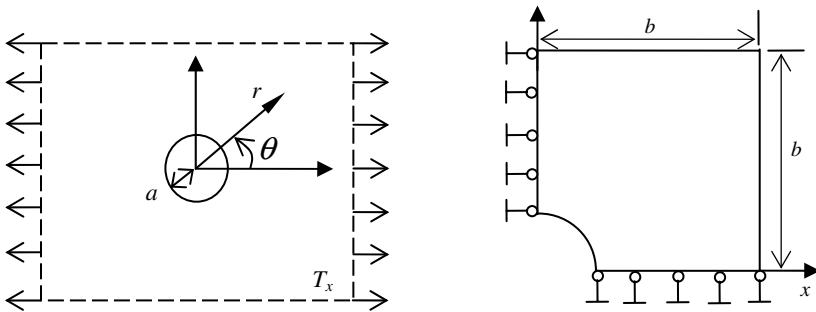

Fig. 7. Infinite two-dimensional solid with a circular hole subjected to a tensile force and its quarter model.

Goodier (1970)].

$$\sigma_{xx} = T_x \left\{ 1 - \frac{a^2}{r^2} \left[\frac{3}{2} \cos(2\theta) + \cos(4\theta) \right] + \frac{3a^4}{2r^4} \cos(4\theta) \right\}, \tag{48}$$

$$\sigma_{yy} = -T_x \left\{ \frac{a^2}{r^2} \left[\frac{1}{2} \cos(2\theta) - \cos(4\theta) \right] + \frac{3a^4}{2r^4} \cos(4\theta) \right\}, \tag{49}$$

$$\sigma_{xy} = -T_x \left\{ \frac{a^2}{r^2} \left[\frac{1}{2} \sin(2\theta) + \sin(4\theta) \right] - \frac{3a^4}{2r^4} \sin(4\theta) \right\}, \tag{50}$$

where (r, θ) are the polar coordinates and θ is measured counterclockwise from the positive x-axis. Traction boundary conditions are imposed on the right and the upper edges based on the analytical solutions in the above equations. The displacement components corresponding to the stress are expressed as

$$u_r = \frac{T_x}{4\mu} \left\{ r \left[\frac{(\kappa - 1)}{2} + \cos(2\theta) \right] + \frac{a^2}{r} \left[1 + (1 + \kappa) \cos(2\theta) \right] - \frac{a^4}{r^3} \cos(2\theta) \right\}, \tag{51}$$

$$u_\theta = \frac{T_x}{4\mu} \left[(1 - \kappa) \frac{a^2}{r} - r - \frac{a^4}{r^3} \right] \sin(2\theta), \tag{52}$$

where

$$\mu = \frac{E}{2(1 + v)}, \quad \kappa = \begin{cases} 3 - 4v, & \text{Plane strain} \\ \dfrac{3 - v}{1 + v}, & \text{Plane stress.} \end{cases} \tag{53}$$

The parameters in this problem are taken as $E = 3.0 \times 10^7$, $v = 0.3$, $a = 1$, $b = 5$ and $T_x = 10$.

We study this problem using FEM, LC-PIM and LC-RPIM with four models of irregular nodes distributions (577, 1330, 2850 and 3578 nodes). The convergence rates in both displacement norm and energy norm are showed in Fig. 8. Similar conclusion can be drawn as previous example, the LC-RPIM obtains almost-equal convergence rate in displacement rate compared with FEM and LC-PIM. However, the LC-RPIM and LC-PIM achieve better accuracy and higher convergence rates in energy norm, which are 1.22 and 1.40 respectively for this particular problem.

Figure 9 plots the values of strain energy of each model against the DOF for all the three methods used. Again, it can be observed that the LC-RPIM, similar as the LC-PIM, provides an upper bound solution in energy norm and the LC-RPIM is tighter than the LC-PIM to the reference value of strain energy.

4.4. *2D square plate subjected to uniform pressure and body force*

As shown in Fig. 10, a 2D square plate is studied. The plate is constrained on the left, the right and the bottom edges, and subjected to uniform pressure $(1\,\text{N/m})$ and a uniformly distributed body force of $b^T = \{0 \quad -1\}$. We consider this problem as plane stress with the following parameters: $E = 3.0 \times 10^7$ and $\nu = 0.3$.

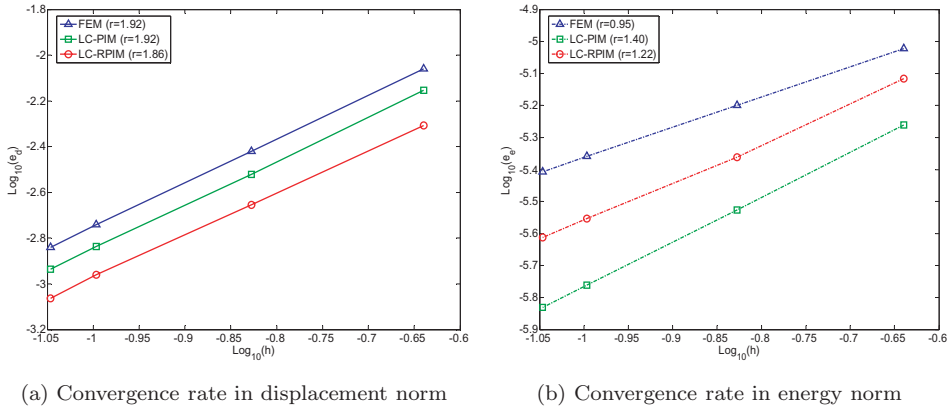(a) Convergence rate in displacement norm   (b) Convergence rate in energy norm

Fig. 8. Comparison of convergence rate between the linear FEM, the LC-PIM and the LC-RPIM via the 2D infinite plate with hole.
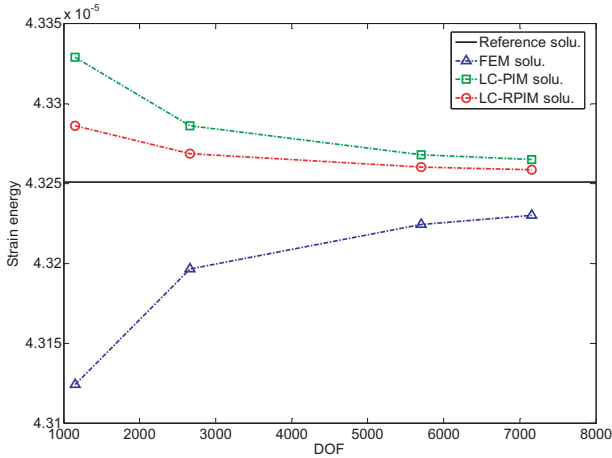

Fig. 9. Upper bound solution obtained using the LC-RPIM and LC-PIM for the 2D infinite plate with hole; The lower bound solution is obtained using the FEM with linear elements.

The problem is discretized with four models of regular nodes distribution (41, 145, 545 and 2113 nodes). We also investigated the upper bound property of LC-RPIM. As the analytical solution for this problem is not available, a reference solution is obtained by using the FEM with a very fine mesh (8238 nodes). Figure 11 shows the calculated strain energies against the DOF, and it can be observed again that the LC-RPIM gives an upper bound solution and is tighter than the LC-PIM.

4.5. *2D automotive part: Rim*

A typical rim of automotive component is studied here. As shown in Fig. 12, the rim is fixed at the nodes located along the inner circle and a pressure of 100 is applied along the lower arc edge within the angle of 60°.
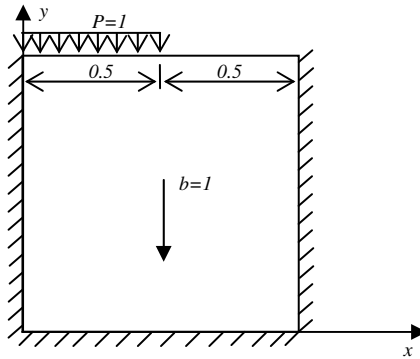
Fig. 10. A square plate subjected to uniform pressure and a uniformly distributed body force.
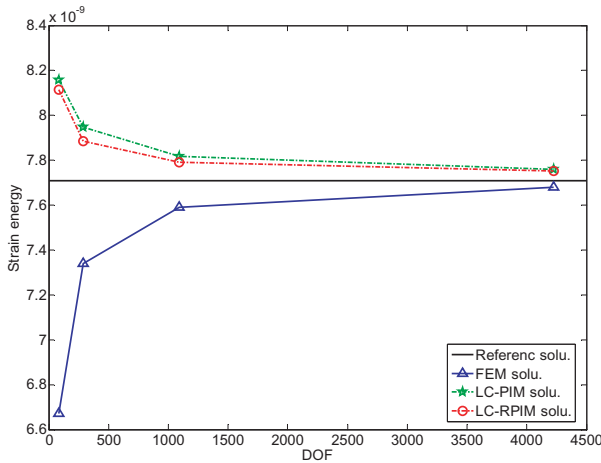

Fig. 11. Upper bound solution obtained using the LC-RPIM and LC-PIM for the 2D square plate problem. The lower bound solution is obtained using the FEM with linear elements.

This problem is studied by using LC-RPIM, LC-PIM and FEM with four models of nodes distributions, i.e. 611, 935, 1192 and 2608 nodes. Against the DOF, strain energies of the numerical solutions provided by the three methods are plotted in Fig. 13, in which the reference strain energy is obtained by using the FEM with very fine mesh (9835 nodes). The picture shows that the compatible FEM model provides lower bound, LC-RPIM and LC-PIM both provide upper bound in strain energy and the upper bound of LC-RPIM solution is much tighter than that of LC-PIM solution.

4.6. *3D lame problem*

Finally, a three-dimensional Lame problem is studied, which consists of hollow sphere with inner radius a, outer radius b and subjected to internal pressure p,
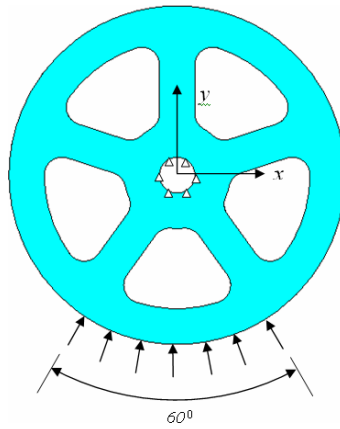
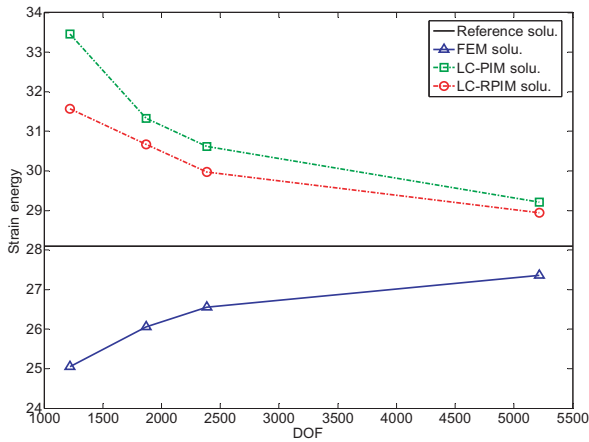Fig. 12. Model of an automotive rim.

Fig. 13. Upper bound solution obtained using the LC-RPIM and LC-PIM for the problem of 2D rim. The lower bound solution is obtained using the FEM with linear elements.

as shown in Fig. 14. The analytical solution is available for this problem in polar coordinate system [Timoshenko and Goodier (1970)].

$$u_r = \frac{Pa^3 r}{E(b^3 - a^3)} \left[(1 - 2\nu) + (1 + \nu) \frac{b^3}{2r^3} \right], \tag{54}$$

$$\sigma_r = \frac{Pa^3 (b^3 - r^3)}{r^3 (a^3 - b^3)}, \tag{55}$$

$$\sigma_\theta = \frac{Pa^3 (b^3 + 2r^3)}{2r^3 (b^3 - a^3)}, \tag{56}$$
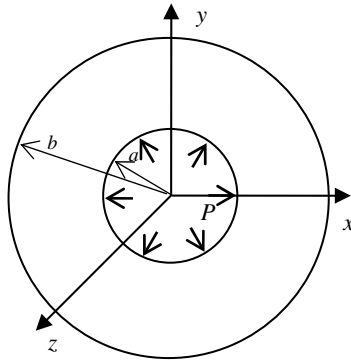
Fig. 14. The 3D Lame problem of a hollow sphere subjected to an internal pressure.
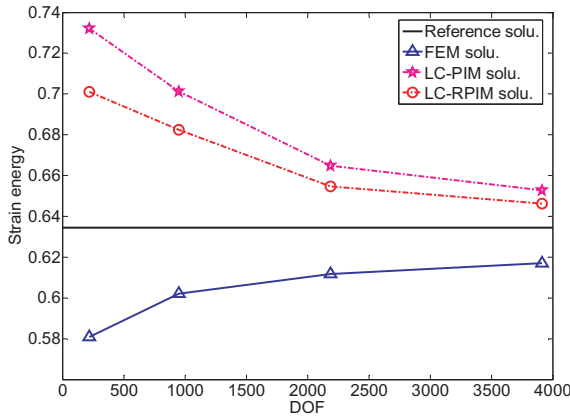

Fig. 15. Upper bound solution obtained using the LC-RPIM and LC-PIM for the problem of 3D Lame problem. The lower bound solution is obtained using the FEM with linear elements.

where r is the radial distance from the centroid of the sphere to the point of interest in the sphere. As the problem is spherically symmetrical, one-eight of the sphere is modeled and symmetry boundary conditions are applied on the three planes of symmetry. The parameters are taken as $E = 1.0$, $v = 0.3$, $a = 1$, $b = 2$ and $P = 1$.

The problem is presented using four models of nodes distributions, i.e. 173, 317, 729 and 1304 nodes. Values of the calculated strain energy for FEM, LC-PIM and LC-RPIM are plotted against the DOF in Fig. 15. For this 3D problem, LC-RPIM is found producing an upper bound solution, and is tighter than the LC-PIM.

5. Conclusions

In this work, a study on the upper bound property of the linearly conforming radial point interpolation method (LC-RPIM) has been conducted. In a summary, some

conclusions are drawn as follows:

- The LC-RPIM is variationally consistent, and the generalized Galerkin weak form, which can be derived from the Hellinger–Reissner's two-field variational principle, is a valid weak form for the LC-RPIM.
- Compared with the linear FEM and LC-PIM using linear interpolation, the LC-RPIM obtains similar accuracy and convergence rate in displacement norm.
- LC-RPIM performs as a combination of compatible model and equilibrium model. Therefore, the convergence rate in energy norm for the LC-RPIM is, in theory, between 1.0 and 2.0, which is similar to the LC-PIM and higher than the linear FEM.
- LC-RPIM provides an upper bound solution in energy norm to elasticity problems except a few trivial cases.
- Compared with LC-PIM which can also provide upper bound to elasticity problems, upper bound of LC-RPIM solution is much tighter than that of LC-PIM.

References

Chen, J. S., Wu, C. T., Yoon, S. and You, Y. [2001] A stabilized conforming nodal integration for Galerkin mesh-free methods, *Int. J. Numer. Meth. Eng.* **50**, 435–466.

Golberg, M. A., Chen, C. S. and Bowman, H. [1999] Some recent results and proposals for the use of radial basis functions in the BEM, *Eng. Anal. Bound. Elem.* **23**, 285–296.

Hardy, R. L. [1990] Theory and applications of the multiquadrics-biharmonic method (20 years of discovery 1968–1988), *Computers & Mathematics with Applications* **19**, 163–208.

Liu, G. R. and Gu, Y. T. [1999] A point interpolation method, In *Proc 4th Asia-Pacific Conference on Computational Mechanics*, December, Singapore, 1009–1014.

Liu, G. R. and Gu, Y. T. [2001] A point interpolation method for two-dimensional solids, *Int. J. Numer. Meth. Eng.* **50**, 937–951.

Liu, G. R. [2002] *Meshfree Methods: Moving Beyond the Finite Element Method* (CRC Press, Boca Raton, USA).

Liu, G. R. and Gu, Y. T. [2005] *An Introduction to Meshfree Methods and Their Programming* (Springer, Dordrecht, The Netherlands).

Liu, G. R., Zhang, G. Y., Dai, K. Y., Wang, Y. Y., Zhong, Z. H., Li, G. Y. and Han, X. [2005a] A linearly conforming point interpolation method (LC-PIM) for 2D solid mechanics problems, *Int. J. Comput. Meth.* **2**(4), 645–665.

Liu, G. R., Zhang, G. Y., Gu, Y. T. and Wang, Y. Y. [2005b] A meshfree radial point interpolation method (RPIM) for three-dimensional solids, *Comput. Mech.* **36**(6), 421–430.

Liu, G. R., Li, Y., Dai, K. Y., Luan, M. Y. and Xue, W. [2006] A linearly conforming RPIM for 2D solid mechanics, *Int. J. Comput. Meth.* **3**(4), 401–428.

Liu, G. R. and Zhang, G. Y. [2007] Upper bound solution to elasticity problems: A unique property of the linearly conforming point interpolation method (LC-PIM), *Int. J. Numer. Meth. Eng.*, in press.

Timoshenko, S. P. and Goodier, J. N. [1970] *Theory of Elasticity*, 3rd edn. (McGraw-Hill, New York).

Wang, J. G. and Liu, G. R. [2000] Radial point interpolation method for elastoplastic problem, *1st International Conference on Structural Stability and Dynamics*, December 7–9, Taipei, Taiwan: 703–708.

Wang, J. G. and Liu, G. R. [2002a] A point interpolation meshless method based on radial basis functions, *Int. J. Numer. Meth. Eng.* **54**, 1623–1648.

Wang, J. G. and Liu, G. R. [2002b] On the optimal shape parameters of radial basis functions used for 2-D meshless methods, *Comput. Method Appl. M.* **191**, 2611–2630.

Wu, H. C. [1982] *Variational Principle in Elasticity and Applications* (Scientific Press, Beijing).